

UNIVERSIDAD DE CONCEPCIÓN



CENTRO DE INVESTIGACIÓN EN  
INGENIERÍA MATEMÁTICA (CI<sup>2</sup>MA)



**Spectral WENO schemes with adaptive mesh refinement for  
models of polydisperse sedimentation**

RAIMUND BÜRGER, PEP MULET,  
LUIS M. VILLADA

PREPRINT 2011-30

SERIE DE PRE-PUBLICACIONES



---

# Spectral WENO schemes with Adaptive Mesh Refinement for models of polydisperse sedimentation

Raimund Bürger<sup>1,\*</sup>, Pep Mulet<sup>2,\*\*</sup>, and Luis Miguel Villada<sup>1,\*\*\*</sup>

<sup>1</sup> CI<sup>2</sup>MA and Departamento de Ingeniería Matemática, Facultad de Ciencias Físicas y Matemáticas, Universidad de Concepción, Casilla 160-C, Concepción, Chile.

<sup>2</sup> Departament de Matemàtica Aplicada, Universitat de València, Av. Dr. Moliner 50, E-46100 Burjassot, Spain.

**Key words** Systems of conservation laws, sedimentation of polydisperse suspensions, shock-capturing schemes, Adaptive Mesh Refinement

**MSC (2000)** 76M20, (35L65, 65M06, 76T20)

*This is paper is dedicated to Professor Wolfgang L. Wendland on the occasion of his 75th birthday.*

The sedimentation of a polydisperse suspension with particles belonging to  $N$  size classes (species) can be described by a system of  $N$  nonlinear, strongly coupled scalar first-order conservation laws. Its solutions usually exhibit kinematic shocks separating areas of different composition. Based on the so-called secular equation [J.Anderson, Lin. Alg. Appl. **246**, 49–70 (1996)], which provides access to the spectral decomposition of the Jacobian of the flux vector for this class of models, Bürger et al. [J. Comput. Phys. **230**, 2322–2344 (2011)] proposed a spectral weighted essentially non-oscillatory (WENO) scheme for the numerical solution of the model. It is demonstrated that the efficiency of this scheme can be improved by the technique of Adaptive Mesh Refinement (AMR), which concentrates computational effort on zones of strong variation. Numerical experiments for the cases  $N = 4$  and  $N = 7$  are presented.

## 1 Introduction

### 1.1 Scope

The sedimentation of a polydisperse suspension of small rigid spheres of the same density that belong to a finite number  $N$  of species differing in size can be described by a spatially one-dimensional system of first-order nonlinear conservation laws

$$\partial_t \Phi + \partial_x \mathbf{f}(\Phi) = 0, \quad \Phi = (\phi_1, \dots, \phi_N)^T, \quad \mathbf{f}(\Phi) = (f_1(\Phi), \dots, f_N(\Phi))^T; \quad t > 0, \quad x \in I \subset \mathbb{R}. \quad (1.1)$$

The unknowns are the volume fractions (concentrations)  $\phi_i$  of species  $i$ ,  $i = 1, \dots, N$ , as functions of depth  $x$  and time  $t$ . The flux density functions  $f_i$  are given by  $f_i(\Phi) = \phi_i v_i(\Phi)$ , where  $v_i = v_i(\Phi)$  is the phase velocity of particle species  $i$  that is assumed to be given as an explicit function of  $\Phi$ . The model (1.1) and its variants are widely used in applications including wastewater treatment, mineral processing, chemical engineering and volcanology. Moreover, a very similar model describes multi-class traffic flow. See [5, 7, 10, 13] for references.

Typical solutions of (1.1), for instance for batch settling of an initially homogeneous suspension in a column, include moving and stationary discontinuities (kinematic shocks) separating areas of different composition. The accurate numerical approximation of these solutions is a challenge since closed-form eigenvalues and eigenvectors of the flux Jacobian  $\mathcal{J}_{\mathbf{f}}(\Phi) = (f_{ij}(\Phi))_{1 \leq i, j \leq N} := (\partial f_i(\Phi) / \partial \phi_j)_{1 \leq i, j \leq N}$  are usually not available, and the characteristic fields are neither genuinely nonlinear nor linearly degenerate. Some of these sedimentation models, including the widely used models by Masliyah, Lockett and Bassoon (MLB model) [21, 22] and Höfler and Schwarzer (HS model) [16], give rise to flux Jacobians whose eigenstructure can be analyzed through a convenient hyperbolicity criterion that has become known as the “secular equation” [1, 6]. When this approach applies, hyperbolicity can be ensured under easily verifiable conditions and the Jacobian eigenstructure can be computed numerically, so that efficient shock capturing schemes may be applied for the numerical computation of the solutions of the models.

---

\* Corresponding author, e-mail: rburger@ing-mat.udec.cl

\*\* e-mail: mulet@uv.es

\*\*\* e-mail: lmvillada@ing-mat.udec.cl

The computational cost of these schemes for obtaining simulations with fine resolution and near to steady states can be quite high, in part due to the costly operations involving the computation of the eigenstructure and the nonlinear reconstructions. Adaptive techniques, as the Adaptive Mesh Refinement (AMR) algorithm [4], aim to reduce the computational cost of these algorithms, by using a higher resolution near salient flow features (shocks, heads and tails of rarefactions, etc.), while employing a coarse mesh near smooth regions of the flow.

In the present work, we apply the AMR technique to two different WENO schemes introduced in [7], namely to a WENO scheme implemented in a component-wise fashion combined with global Lax-Friedrichs flux vector splitting (denoted by ‘‘COMP-GLF’’), and alternatively, to a WENO scheme applied in a characteristic-wise (spectral) fashion, and which makes essential use of the interlacing property of the velocities  $v_1, \dots, v_N$  with the eigenvalues of  $\mathcal{J}_f(\Phi)$  (see Sect. 2.1). The second version is denoted by ‘‘SPEC-INT’’. The scheme COMP-GLF does not rely on characteristic information, is much easier to implement than SPEC-INT, and on a fixed uniform grid is several times faster than SPEC-INT. However, SPEC-INT is substantially more accurate than COMP-GLF, and turns out to be even more efficient than COMP-GLF in terms of reduction of numerical error per CPU time [7]. In the present work it turns out that equipping both versions with AMR produces substantial gains in computational efficiency when compared with the corresponding non-adaptive version, and that the adaptive versions based on SPEC-INT are consistently more efficient than those relying on COMP-GLF.

## 1.2 Related work

Any kind of adaptativity that permits to restrict the use of a high-resolution scheme on a fine grid to a portion of the computational domain will produce a benefit in terms of computational efficiency. Common methods are multiresolution algorithms [11, 12], moving mesh methods [27] and approximations on unstructured meshes [17]. Adaptive Mesh Refinement (AMR) is a grid adaptation technique, introduced by Berger and Olinger [4], which is based not so much on the reduction of the number of cells on the grid as on the reduction of the overall number of applications of the integration algorithm. This algorithm is very time-consuming especially for high-resolution shock capturing schemes. The AMR algorithm is a two-fold adaptive method. The goal of allowing arbitrary grid resolution is attained by the definition of a set of overlapping grids of different resolutions –a grid hierarchy– being the grid at each resolution level defined only on the part of the domain that is foreseen to require such a resolution. The way in which the grids are overlapped allows to refine also in time, in the sense that each grid is integrated with temporal steps adapted to its spatial grid size. This time refinement is another key feature for improving the overall performance of the algorithm [3, 4].

## 1.3 Outline of the paper

The remainder of the paper is organized as follows. In Section 2 we outline some preliminaries. Specifically, in Section 2.1 we review the MLB model of polydisperse sedimentation and recall in Section 2.2 the basic hyperbolicity results from [6, 13] based on the secular equation [1]. In Section 3 we describe the numerical techniques that are used in this paper, namely the SPEC-INT and COMP-GLF schemes from [7] (Sect. 3.1) and the main building blocks of an AMR algorithm (Sect. 3.2) following [2]. The combination of both types of schemes with the AMR technique gives rise to schemes denoted by SPEC-INT-AMR and COMP-GLF-AMR, whose performance is illustrated by numerical examples in Section 4.

# 2 Preliminaries

## 2.1 Sedimentation of polydisperse suspensions

The MLB model arises from the continuity and linear momentum balance equations for the solid species and the fluid through suitable constitutive assumptions and simplifications. We refer to [5, 9] for details and introduce the model here in its final form. For particles that have the same density, the velocities  $v_1, \dots, v_N$  are given by

$$v_i(\Phi) := \frac{(\varrho_s - \varrho_f)gd_1^2}{18\mu_f}(1 - \phi)V(\phi)(\delta_i - \boldsymbol{\delta}^T \Phi), \quad i = 1, \dots, N, \quad (2.1)$$

where  $d_1 > d_2 > \dots > d_N$  are the respective species diameters,  $\delta_i = d_i^2/d_1^2$ ,  $\boldsymbol{\delta} = (\delta_1 = 1, \delta_2, \dots, \delta_N)^T$ ,  $\varrho_s$  and  $\varrho_f$  are the solid and fluid densities,  $g$  is the acceleration of gravity,  $\mu_f$  is the fluid viscosity,  $\phi = \phi_1 + \dots + \phi_N$  is the total solids volume fraction, and  $V = V(\phi)$  is the collective hindered settling factor that is assumed to satisfy  $V(0) = 1$ ,  $V(\phi_{\max}) = 0$  and  $V'(\phi) \leq 0$  for  $\phi \in [0, \phi_{\max}]$ , where the constant  $\phi_{\max}$  denotes the maximum total solids concentration. A standard choice for  $V(\phi)$  is the equation [24]

$$V(\phi) = (1 - \phi)^{n_{\text{RZ}} - 2} \quad \text{if } \Phi \in \mathcal{D}_{\phi_{\max}}, n_{\text{RZ}} > 2; \quad V(\phi) = 0 \quad \text{otherwise.} \quad (2.2)$$

The components  $f_1(\Phi), \dots, f_N(\Phi)$  of the flux vector  $\mathbf{f}(\Phi)$  of the MLB model are given by

$$f_i(\Phi) := v_i(\mathbf{0})\phi_i(1-\phi)V(\phi)(\delta_i - \delta^T\Phi), \quad i = 1, \dots, N. \quad (2.3)$$

## 2.2 Secular equation and hyperbolicity analysis

For general kinematic models with  $v_i = v_i(\phi_1, \dots, \phi_N)$ , the Jacobian  $\mathcal{J}_f(\Phi)$  has no definite structure, hence its spectral information cannot be readily obtained. However, when the velocities  $v_1, \dots, v_N$  do not depend on each of the  $N$  components of  $\Phi$  in an individual way, but are rather functions of a small number  $m \ll N$  of scalar functions of  $\Phi$  (as is the case of the MLB model), i.e.,  $v_i = v_i(p_1, \dots, p_m)$  and  $p_l = p_l(\Phi)$  for  $i = 1, \dots, N$  and  $l = 1, \dots, m$ , then the entries of  $\mathcal{J}_f(\Phi)$  are given by

$$f_{ij} = \frac{\partial(\phi_i v_i)}{\partial \phi_j} = v_i \delta_{ij} + \sum_{l=1}^m \phi_i \frac{\partial v_i}{\partial p_l} \frac{\partial p_l}{\partial \phi_j}, \quad i, j = 1, \dots, N, \quad (2.4)$$

i.e.,  $\mathcal{J}_f(\Phi)$  is a rank- $m$  perturbation of the diagonal matrix  $\mathbf{D} := \text{diag}(v_1, \dots, v_N)$  of the form  $\mathcal{J}_f = \mathbf{D} + \mathbf{B}\mathbf{A}^T$ , where

$$\mathbf{B} := (B_{il}) = (\phi_i \partial v_i / \partial p_l), \quad \mathbf{A} := (A_{jl}) = (\partial p_l / \partial \phi_j), \quad 1 \leq i, j \leq N, \quad 1 \leq l \leq m. \quad (2.5)$$

The hyperbolicity analysis is then based on the following theorem, which can be found in [1], but we give here the form in [13], which provides the explicit formulas to be used in the applications.

**Theorem 2.1** (The secular equation, [1, 13]) *Assume that  $v_i > v_j$  for  $i < j$ , and that  $\mathbf{A}$  and  $\mathbf{B}$  have the formats specified in (2.5). We denote by  $S_r^p$  the set of all (ordered) subsets of  $r$  elements taken from a set of  $p$  elements. If  $\mathbf{X}$  is an  $m \times N$  matrix,  $I := \{i_1 < \dots < i_k\} \in S_k^N$  and  $J := \{j_1 < \dots < j_l\} \in S_l^m$ , then we denote by  $\mathbf{X}^{I,J}$  the  $k \times l$  submatrix of  $\mathbf{X}$  given by  $(\mathbf{X}^{I,J})_{p,q} = X_{i_p, j_q}$ . Let  $\lambda \neq v_i$  for  $i = 1, \dots, N$ . Then  $\lambda$  is an eigenvalue of  $\mathbf{D} + \mathbf{B}\mathbf{A}^T$  if and only if*

$$R(\lambda) := \det(\mathbf{I} + \mathbf{A}^T(\mathbf{D} - \lambda\mathbf{I})^{-1}\mathbf{B}) = 1 + \sum_{i=1}^N \frac{\gamma_i}{v_i - \lambda} = 0. \quad (2.6)$$

The relation  $R(\lambda) = 0$  is known as the secular equation [1]. The coefficients  $\gamma_i$  are given by the following expression:

$$\gamma_i = \sum_{r=1}^{\min\{N, m\}} \sum_{I \in S_r^N, J \in S_r^m} \frac{\det \mathbf{A}^{I,J} \det \mathbf{B}^{I,J}}{\prod_{l \in I, l \neq i} (v_l - v_i)}, \quad i = 1, \dots, N. \quad (2.7)$$

When  $m \leq 2$ , the quantities (2.7) can be easily computed and the hyperbolicity analysis via the secular equation is much less involved than discussing the zeros of  $\det(\mathcal{J}_f(\Phi) - \lambda\mathbf{I})$ , as was done in [5, 25]. For  $m = 3$  or  $m = 4$ , the computations are more involved [6, 8], but have turned out very useful in providing at least partial results concerning hyperbolicity, where the theoretical analysis of  $\det(\mathcal{J}_f(\Phi) - \lambda\mathbf{I})$  is essentially out of reach. For the special case of the MLB model with equal-density spheres, one can identify the dependence of  $v_i$  on the parameters  $p_1 := \phi$  and  $p_2 := \delta^T\Phi$ . Therefore, we are in the case  $m = 2$  and we can compute explicitly the coefficients  $\gamma_i = -v_1(\mathbf{0})(n-1)(1-\phi)^{n-2}\phi_i\delta_i > 0$  if  $\phi_i > 0$  and  $\phi < 1$ .

The following corollary illustrates the importance of the secular equation. Its proof (see [6]) follows from Theorem 2.1 by a discussion of the poles of  $R(\lambda)$  and its asymptotic behavior as  $\lambda \rightarrow \pm\infty$ .

**Corollary 2.1** ([6]) *With the notation of Theorem 2.1, assume that  $\gamma_i \cdot \gamma_j > 0$  for  $i, j = 1, \dots, N$ . Then  $\mathbf{D} + \mathbf{B}\mathbf{A}^T$  is diagonalizable with real eigenvalues  $\lambda_1, \dots, \lambda_N$ . If  $\gamma_1, \dots, \gamma_N > 0$ , the following so-called interlacing property holds:*

$$v_N < \lambda_N < v_{N-1} < \lambda_{N-1} < \dots < v_1 < \lambda_1 < M_2 := v_1 + \gamma_1 + \dots + \gamma_N. \quad (2.8)$$

As a consequence, we see that the model (1.1) with the flux vector  $\mathbf{f}(\Phi)$  of the MLB model given by (2.3) is strictly hyperbolic if  $\phi_1 > 0, \dots, \phi_N > 0$  and  $\phi < \phi_{\max} < 1$ .

## 3 Numerical schemes

### 3.1 SPEC-INT and COMP-GLF schemes

It is well known that nonlinear hyperbolic systems of conservation laws of the type (1.1) can develop discontinuities (shocks), even for smooth initial data. By Lax-Wendroff's theorem [19], conservative schemes can cope with this situation

since their limits are weak solutions of the conservation law. For grid points  $x_i = i\Delta x$ ,  $t_n = n\Delta t$ , a conservative scheme for  $\Phi_i^n \approx \Phi(x_i, t_n)$  is given by

$$\Phi_i^{n+1} = \Phi_i^n - \frac{\Delta t}{\Delta x} (\hat{\mathbf{f}}_{i+1/2} - \hat{\mathbf{f}}_{i-1/2}), \quad \hat{\mathbf{f}}_{i+1/2} = \hat{\mathbf{f}}(\Phi_{i-s+1}^n, \dots, \Phi_{i+s}^n), \quad i \in \mathbb{Z}.$$

The key point is the design of the numerical flux  $\hat{\mathbf{f}}_{i+1/2}$  so that resulting scheme is (at least second-order) accurate and stable. The most common approach for the design of numerical fluxes is to solve Riemann problems, either exactly (as in the original Godunov scheme, which is very costly), or approximately (e.g., as in the Roe scheme). For polydisperse sedimentation, using exact Riemann solvers is out of reach, since the eigenstructure of the flux Jacobian is hard to compute.

In [5], the authors used central schemes [18] for the MLB model. In [7] we used Shu-Osher's technique [26] (also used in [10]) along with the information provided by the secular equation to get efficient schemes for polydisperse sedimentation based on MLB and HS models. We here briefly describe this scheme, which is based on the method of lines, that is, on applying an ODE solver to a spatially semi-discretized equations. For the discretization of the flux derivative we use local characteristic projections. Local characteristic information to compute  $\hat{\mathbf{f}}_{i+1/2}$  is provided by the eigenstructure of  $\mathcal{J}_{\mathbf{f}}(\Phi_{i+1/2})$ , where  $\Phi_{i+1/2} = \frac{1}{2}(\Phi_i + \Phi_{i+1})$ , given by the right and left eigenvectors,  $\mathbf{r}_{i+1/2,j}$  and  $\mathbf{l}_{i+1/2,j}$ , respectively, that form the respective matrices

$$\mathbf{R}_{i+1/2} = [\mathbf{r}_{i+1/2,1} \quad \dots \quad \mathbf{r}_{i+1/2,N}], \quad (\mathbf{R}_{i+1/2}^{-1})^T = [\mathbf{l}_{i+1/2,1} \quad \dots \quad \mathbf{l}_{i+1/2,N}].$$

From a local flux-splitting  $\mathbf{f}^{\pm,k}$  (we omit its dependency on  $i+1/2$ ) given by  $\mathbf{f}^{-,k} + \mathbf{f}^{+,k} = \mathbf{f}$ , where  $\pm\lambda_k(\mathcal{J}_{\mathbf{f}^{\pm,k}}(\Phi)) \geq 0$ ,  $\Phi \approx \Phi_{i+1/2}$  and  $\lambda_k$  is the  $k$ -th eigenvalue,  $k = 1, \dots, N$ , we can define the  $k$ -th characteristic flux as

$$g_j^{\pm,k} = \mathbf{l}_{i+1/2,k}^T \cdot \mathbf{f}^{\pm,k}(\Phi_j).$$

If  $\mathcal{R}^+$  and  $\mathcal{R}^-$  denote upwind-based reconstructions, then

$$\begin{aligned} \hat{g}_{i+1/2,k} &= \mathcal{R}^+(g_{i-s+1}^{+,k}, \dots, g_{i+s-1}^{+,k}; x_{i+1/2}) + \mathcal{R}^-(g_{i-s+2}^{-,k}, \dots, g_{i+s}^{-,k}; x_{i+1/2}), \\ \hat{\mathbf{f}}_{i+1/2} &= \mathbf{R}_{i+1/2} \hat{\mathbf{g}}_{i+1/2} = \sum_{k=1}^n \hat{g}_{i+1/2,k} \mathbf{r}_{i+1/2,k}. \end{aligned}$$

If we do not want to use local characteristic information, we can use the previous formula with  $\mathbf{R}_{i+1/2} = \mathbf{I}_N$ , where  $\mathbf{I}_N$  denotes the  $N \times N$  identity matrix, and a global flux splitting  $\mathbf{f}^- + \mathbf{f}^+ = \mathbf{f}$ , where  $\pm\lambda_k(\mathcal{J}_{\mathbf{f}^{\pm}}(\Phi))' \geq 0$  for all  $k$ . With this choice, and denoting by  $\mathbf{e}_k$  the  $k$ th unit vector, we get  $\mathbf{g}_j^{\pm,k} = \mathbf{e}_k^T \mathbf{f}^{\pm}(\Phi_j) = f_k^{\pm}(\Phi_j)$ , i.e.,  $\mathbf{g}_j^{\pm,k}$  are the components of the split fluxes, and the numerical flux is computed component by component by reconstructing the split fluxes component by component, i.e.,  $\hat{\mathbf{f}}_{i+1/2} = (\hat{f}_{i+1/2,1}, \dots, \hat{f}_{i+1/2,N})^T$ , where

$$\hat{f}_{i+1/2,k} = \mathcal{R}^+(g_{i-s+1}^{+,k}, \dots, g_{i+s-1}^{+,k}; x_{i+1/2}) + \mathcal{R}^-(g_{i-s+2}^{-,k}, \dots, g_{i+s}^{-,k}; x_{i+1/2}), \quad k = 1, \dots, N.$$

This scheme will be referred to as COMP-GLF and it is a high-order extension of the Lax-Friedrichs scheme.

We now explain the SPEC-INT scheme. If  $\lambda_k(\mathcal{J}_{\mathbf{f}}(\Phi)) > 0$  (respectively,  $< 0$ ) for all  $\Phi \in [\Phi_i, \Phi_{i+1}]$ , where  $[\Phi_i, \Phi_{i+1}] \subset \mathbb{R}^N$  denotes the segment joining both states, then we upwind (since then there is no need for flux splitting):

$$\mathbf{f}^{+,k} = \mathbf{f}, \quad \mathbf{f}^{-,k} = 0 \quad \text{if } \lambda_k(\mathcal{J}_{\mathbf{f}}(\Phi)) > 0, \quad \mathbf{f}^{+,k} = 0, \quad \mathbf{f}^{-,k} = \mathbf{f} \quad \text{if } \lambda_k(\mathcal{J}_{\mathbf{f}}(\Phi)) < 0.$$

On the other hand, if  $\lambda_k(\mathcal{J}_{\mathbf{f}}(\Phi))$  changes sign on  $[\Phi_i, \Phi_{i+1}]$ , then we use a Local Lax-Friedrichs flux splitting given by  $\mathbf{f}^{\pm,k}(\Phi) = \mathbf{f}(\Phi) \pm \alpha_k \Phi$ , where the numerical viscosity parameter  $\alpha_k$  should satisfy

$$\alpha_k \geq \max_{\Phi \in [\Phi_i, \Phi_{i+1}]} |\lambda_k(\mathcal{J}_{\mathbf{f}}(\Phi))|. \quad (3.1)$$

The usual choice of the numerical viscosity

$$\alpha_k = \max\{|\lambda_k(\mathcal{J}_{\mathbf{f}}(\Phi_i))|, |\lambda_k(\mathcal{J}_{\mathbf{f}}(\Phi_{i+1}))|\}.$$

produces oscillations in the numerical solution indicating that the amount of numerical viscosity is insufficient. The right-hand side of (3.1) can usually not be evaluated exactly since closed-form expressions for the eigenvalues are not available. However, for the present class of models, we may use the interlacing property (see Corollary 2.1) to generate a fairly sharp

bound of that expression. In the case of the MLB model, we have  $\gamma_k < 0$  (see [6, 13]) and the interlacing property can be written as  $v_{k+1}(\Phi) \leq \lambda_k(\Phi) \leq v_k(\Phi)$  for  $k = 1, \dots, N$ , so we have  $|\lambda_k(\Phi)| \leq \max\{|v_k(\Phi)|, |v_{k+1}(\Phi)|\}$  and therefore we can get efficiently computable bounds

$$\max_{\Phi \in [\Phi_i, \Phi_{i+1}]} |\lambda_k(\Phi)| \leq \alpha_k := \max \left\{ \max_{\Phi \in [\Phi_i, \Phi_{i+1}]} |v_k(\Phi)|, \max_{\Phi \in [\Phi_i, \Phi_{i+1}]} |v_{k+1}(\Phi)| \right\}, \quad k = 1, \dots, N. \quad (3.2)$$

(The same property also holds for other models, under appropriate circumstances [6, 8].) We denote by ‘‘SPEC-INT’’ the scheme for which  $\alpha_1, \dots, \alpha_N$  are defined by (3.2).

### 3.2 Adaptive Mesh Refinement (AMR)

In what follows we describe the main building blocks of the AMR algorithm. We refer to [2] for details. We denote by  $G_0, \dots, G_L$  a 1D grid hierarchy composed by  $L + 1$  grids, such that, except for the coarsest grid  $G_0$ , cells of a given grid are obtained from the subdivision of cells of the immediately coarser grid into  $r$  parts (we assume  $r = 2$ ). The unit interval is thus divided into  $N_0, \dots, N_L$  subintervals of length  $h_l = 1/N_l$ , with  $N_l = 2^l N_0$ ,  $l = 0, \dots, L$ , whose centers will be denoted by  $x_j^l = (j + 1/2)h_l$ ,  $j = 0, \dots, N_l - 1$ ,  $l = 0, \dots, L$ . A ‘‘mesh’’  $G_l$  at resolution level  $l$  is just a subset of the index set  $\{0, \dots, N_l - 1\}$  whose ‘‘extent’’, the union of the cells indexed by elements of  $G_l$ , is denoted by  $\Omega_l(G_l)$ . We consider only ‘‘nested’’ grid hierarchies, i.e.,  $\Omega_l(G_l) \subseteq \Omega_{l-1}(G_{l-1})$  for  $1 \leq l \leq L$  is assumed to hold. We also require that  $\Omega_0(G_0) = \Omega$ .

The meshes will be dynamically updated so that they adapt to the features of the solution, and we denote by  $G_l^{t_l}$  the mesh that corresponds to the resolution level  $l$  and time  $t_l$ . Over each mesh we consider a numerical solution defined by a discrete function  $u_l^{t_l} = (u_{l,j}^{t_l})$ , with  $u_{l,j}^{t_l} \approx u(x_j^l, t_l)$  and  $j \in G_l^{t_l}$ . For given time instant  $t$  we denote  $U^t = \{u_l^t\}$ ,  $0 \leq l \leq L$ .

The algorithm can be described by the time evolution of the meshes and their associated numerical solutions, starting with  $t_l = 0$ ,  $l = 0, \dots, L$  and ending at  $t_l = T$ ,  $l = 0, \dots, L$ , for some  $T > 0$ . The main building blocks of the AMR algorithm — integration and adaptation of the grids and projection from fine to coarse grids — are described next.

We describe now the way the integration of the grids corresponding to the various refinement levels is organized. The first step is to select a time step  $\Delta t_0$  for the coarsest grid, so that the following CFL condition relevant for the grid  $G_0^t$  is satisfied:

$$\Delta t_0 \leq \frac{Ch_0}{\max_{u \in U^t} |f'(u)|}, \quad 0 < C \leq 1.$$

The time steps for the rest of the grids are taken by  $\Delta t_l = \Delta t_{l-1}/2$  for  $l = 1, \dots, L$ , which implies that the equivalent CFL condition holds for each grid. A time step for  $G_0$  corresponds therefore to  $2^l$  time steps for  $G_l$ . The grids are integrated according to the order dictated by the following condition:  $t_{l'} \leq t_l \leq t_{l'} + \Delta t_l$  if  $l \leq l'$ .

At some step of this time evolution,  $(u_l^{t_l+k\Delta t_l}, G_l^{t_l})$ ,  $k = 1, 2$ , are sequentially computed from  $(u_l^{t_l}, G_l^{t_l})$ , supplemented by boundary conditions at a band surrounding  $\Omega_l(G_l^{t_l})$  obtained by interpolation from  $(u_{l-1}^{t_l}, G_{l-1}^{t_l})$  and  $(u_{l-1}^{t_l+2\Delta t_l}, G_{l-1}^{t_l+2\Delta t_l})$ , which must have been computed in previous steps. Once  $(u_l^{t_l+2\Delta t_l}, G_l^{t_l})$  is computed, there is data that overlay  $\Omega_l(G_l^{t_l})$  at different resolution levels. It is at this point that the projection of the data at the fine resolution level should be applied to modify the values  $u_{l-1,j}^{t_l+2\Delta t_l}$  of the immediately coarser grid function that correspond to cells overlaid by cells at  $G_l^{t_l}$  and adjacent to them as well, i.e., such that  $\{2j, 2(j-1), 2(j+1)\} \cap G_l^{t_l} \neq \emptyset$ . In this case, the numerical fluxes corresponding to interfaces of refined coarse cells are modified in such a way that when  $u_{l-1}^{t_l}$  is reintegrated with them, then

$$u_{l-1,j}^{t_l+2\Delta t_l} = \frac{1}{2} (u_{l,2j}^{t_l+2\Delta t_l} + u_{l,2j+1}^{t_l+2\Delta t_l}) \quad \text{if} \quad u_{l-1,j}^{t_l} = \frac{1}{2} (u_{l,2j}^{t_l} + u_{l,2j+1}^{t_l}),$$

i.e., discrete conservation is maintained.

The next issue is the update of the grids. The grids corresponding to the various levels  $G_l$ ,  $1 \leq l \leq L$  have to be modified according to the current characteristics of the flow. The adaptation of each refinement level is performed by discarding the current grid and creating a new one according to specified refinement criteria. In this way, coarsening is not directly performed on refined areas, but implicitly obtained by not refining.

For our cell-centered approach, if  $x_j^l = (j + 1/2)h_l$  is the center of a cell of a grid  $G_l^t$  and  $\mathcal{I}(u_{l-1}^t, x)$  is an interpolation operator (we use a MUSCL interpolator) defined on the data  $u_{l-1}^t = \{u_{l-1,i}^t\}_{i \in G_{l-1}^t}$ , then the cell defined by  $x_j^l$  will be selected for refinement if

$$|u_{l,j}^t - \mathcal{I}(u_{l-1}^t, x_j^l)| > \tau_p \cdot \max_{i,j} |u_{l,i}^t - \mathcal{I}(u_{l-1}^t, x_j^l)|, \quad (3.3)$$

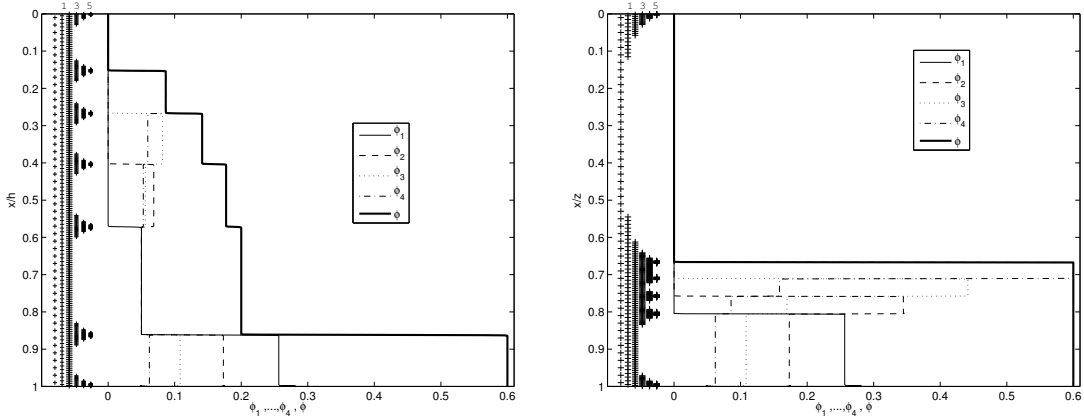


**Fig. 1** Example 1 ( $N = 4$ ): numerical solution obtained with SPEC-INT-AMR with  $L + 1 = 6$  levels with coarsest grid of 50 subintervals at  $t = 50$  s (left) and  $t = 300$  s (right). Here and in Figure 5, the numbers 1, 3 and 5 on the top of the frame bottom represent the level  $l$  of the grid hierarchy.

where  $\tau_p$  is a given tolerance. Note that only the cells present in the current grid are considered for refinement. New cells are included only because of the addition of some extra cells around each marked cell. We also ensure that the refined grid is obtained by subdivision of coarse cells: if a cell  $x_{i,j}^t$  is selected for refinement, then every cell that overlaps the same coarse cell as  $x_{i,j}^t$  is also included in the refined grid. Further, we also include a cell in the refinement list if the modulus of the discrete gradient, computed in the coarser grid, exceeds some large threshold, so that shock formation can be detected from steepened data. For the discrete gradient we use the approximation

$$\frac{\partial u}{\partial x}(x_i^{l-1}, t) \approx \frac{1}{h_{l-1}} \max\{|u_{i-1,i+1}^t - u_{i-1,i}^t|, |u_{i-1,i}^t - u_{i-1,i-1}^t|\}.$$

Once the cells that will compose the refined grid have been selected we add a certain number of extra cells forming a band around each marked cell to ensure that the cells adjacent to a singularity are refined. This device of creating “safety points” follows the spirit of [15, 20, 23]. These extra cells will avoid singularities to escape from the fine grid during one coarse time step. To this aim it would suffice to add a band of one coarse cells around each marked cell. Another criterion for adding cells is dictated by the need of interpolating ghost cell values from *relatively* smooth regions: the length of the stencil of the interpolation operator must be less than twice the length — measured in number of coarse cells — of the band of added cells. In our case we use third-order linear interpolation, and this imposes the addition of two coarse cells at each side of a marked cell. For analogous reasons, if the computation of the numerical flux depends on  $2\mathcal{N}$  values of the fine grid, then, in order to ensure that it is computed using non-interpolated data, the length of the band has to be greater than  $\mathcal{N}/2$ . In the case of the method used in this work, described in Section 3.1, we have  $\mathcal{N} = 3$ , and thus the number of coarse cells added should be at least 2. According to the criteria above, we add two coarse cells in our implementation.

The last observation for this refinement procedure is that it should be performed from fine to coarse resolution levels to ensure that at every moment of the update process it holds that  $\Omega_l(G_l^t) \subseteq \Omega_{l-1}(G_{l-1}^t)$ . We also enforce the inclusion  $\Omega_l(G_l^t) \supseteq \Omega_{l+1}(G_{l+1}^t)$ , so that the whole sequence of grids verifies the desired inclusions. Finally note that the process of computing data at the corresponding surrounding bands is possible because the grids are nested, and this implies that  $\tilde{\Omega}_l(G_l^t) \subseteq \tilde{\Omega}_{l-1}(G_{l-1}^t)$ .

Once the new grid  $\hat{G}_l$  is computed such that  $\Omega_l(\hat{G}_l^t) \subseteq \Omega_{l-1}(G_{l-1}^t)$  is satisfied, one sets

$$\hat{u}_{i,j}^t = \begin{cases} \mathcal{I}(u_{i-1}^t, x_j^l) & \text{if } j \in \hat{G}_l^t \setminus G_l^t, \\ u_{i,j}^t & \text{if } j \in G_l^t, \end{cases}$$

i.e., the value at the  $j$ -th cell is interpolated from data at the next coarser level for cells not in  $G_l^t$ . The refined grid is therefore defined by  $(\hat{G}_l^t, \hat{u}_l^t)$ . Discrete boundary conditions are also applied if the grid overlaps the domain boundary.

## 4 Numerical experiments

The threshold value  $\tau_p$  plays a special role for the performance of the SPEC-INT-AMR and COMP-GLF-AMR methods, since computational time and accuracy are related to their variations. Initially, we perform additional numerical experiments

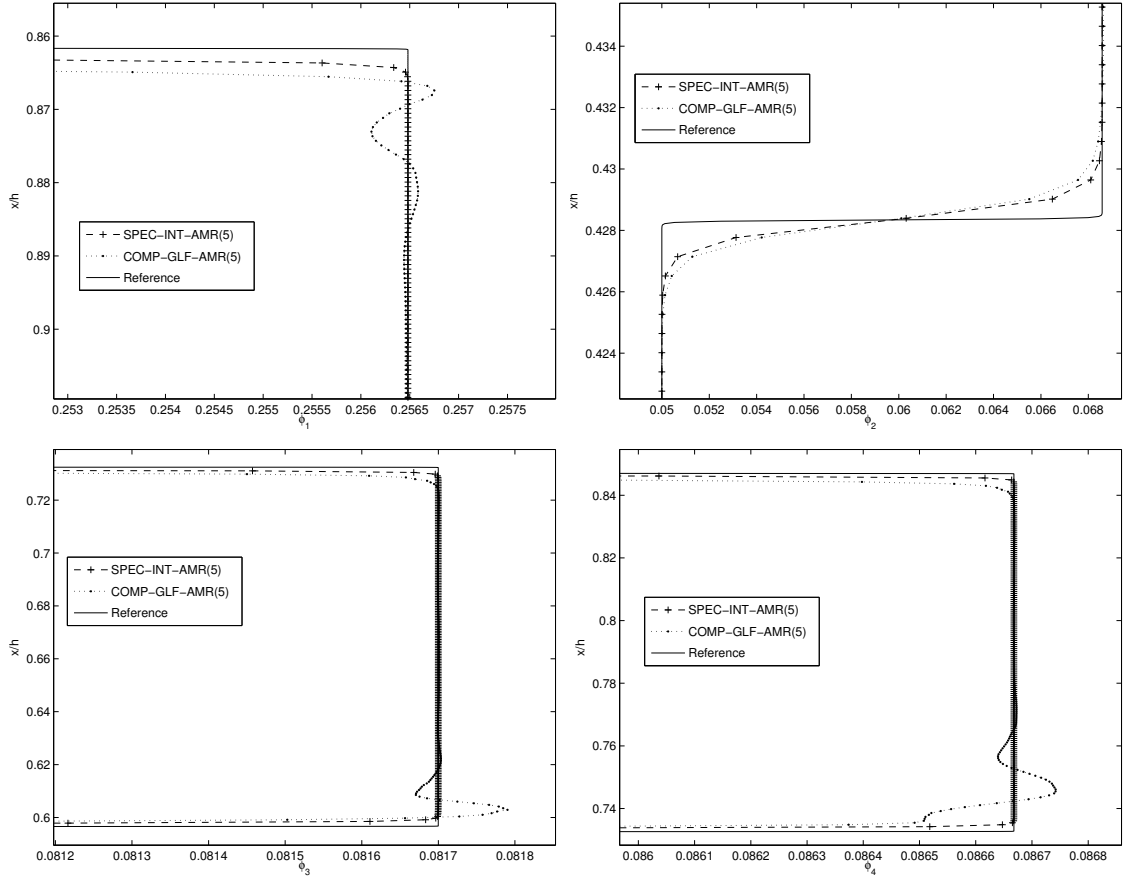


**Fig. 2** Example 1 ( $N = 4$ ): numerical solution at time  $t = 50$  s: details of using SPEC-INT-AMR and COMP-GLF-AMR methods with a grid hierarchy of  $L + 1 = 5$  levels on a coarsest grid with  $N_0 = 50$  subintervals. Here and in Figure 3, the reference solution is computed by SPEC-INT on a fixed grid with  $N_{\text{ref}} = 25600$  subintervals.

based on different examples to solve in order to study the effect of different choices of the parameter  $\tau_p$ . In preliminary computations (not shown here) we tested the values  $\tau_p = 10^{-q}$ ,  $q = 2, 3, 4, 5$ . For  $q = 2$  the AMR schemes turned out to be most efficient in terms of reduction of error per CPU time.

#### 4.1 Example 1 ( $N = 4$ )

As in [6, 7], we consider the standard test case of batch settling of an initially homogeneous suspension in a column characterized by the velocity functions (2.1) with parameters  $N = 4$ ,  $\rho_s = 2790 \text{ kg/m}^3$ ,  $\rho_f = 1208 \text{ kg/m}^3$ ,  $\mu_f = 0.02416 \text{ Pa}\cdot\text{s}$ ,  $g = 9.8 \text{ m/s}^2$ ,  $\delta_1 = 1$ ,  $\delta_2 = 0.64$ ,  $\delta_3 = 0.36$  and  $\delta_4 = 0.16$ . We employ the hindered settling factor (2.2) with exponent  $n_{\text{RZ}} = 4.7$  and initial concentrations  $\phi_i^0 = 0.05$  for  $i = 1, \dots, 4$ .

We simulate the process until the sedimentation process attains a steady state, that is when all particles are captured in a sediment. This sediment usually consists of layers of different composition (which is part of the solution of the problem) separated by stationary kinematic shocks. Figure 1 shows the numerical solution obtained with SPEC-INT-AMR as concentration profiles at two different times together with the corresponding hierarchical grids. We have used a grid hierarchy of  $L + 1 = 6$  levels with a coarsest grid of  $N_0 = 50$  subintervals so that the finest grid has  $N_5 = N_L = 1600$  subintervals. The tolerance for the interpolation error sensor has been set to  $\tau_p = 10^{-2}$ . The plotted positions indicate that the adaptive mesh refinement technique works correctly, in the sense that the scheme correctly detects the formation of shocks and refines the corresponding areas.

In Figures 2 and 3 we compare the results obtained by SPEC-INT-AMR and COMP-GLF-AMR methods with a reference solution computed with SPEC-INT scheme on a fixed uniform grid with  $N_{\text{ref}} = 25600$  subintervals at times  $t = 50$  s and  $t = 300$  s, respectively. We have used a grid hierarchy of  $L + 1 = 5$  levels with a coarsest grid of  $N_0 = 50$  subintervals so that  $N_L = N_4 = 800$ . The tolerance for the interpolation error sensor has been set to  $\tau_p = 10^{-2}$ . The solution of the adaptive computation is mapped to the finest grid using the computed solution where available and by interpolation

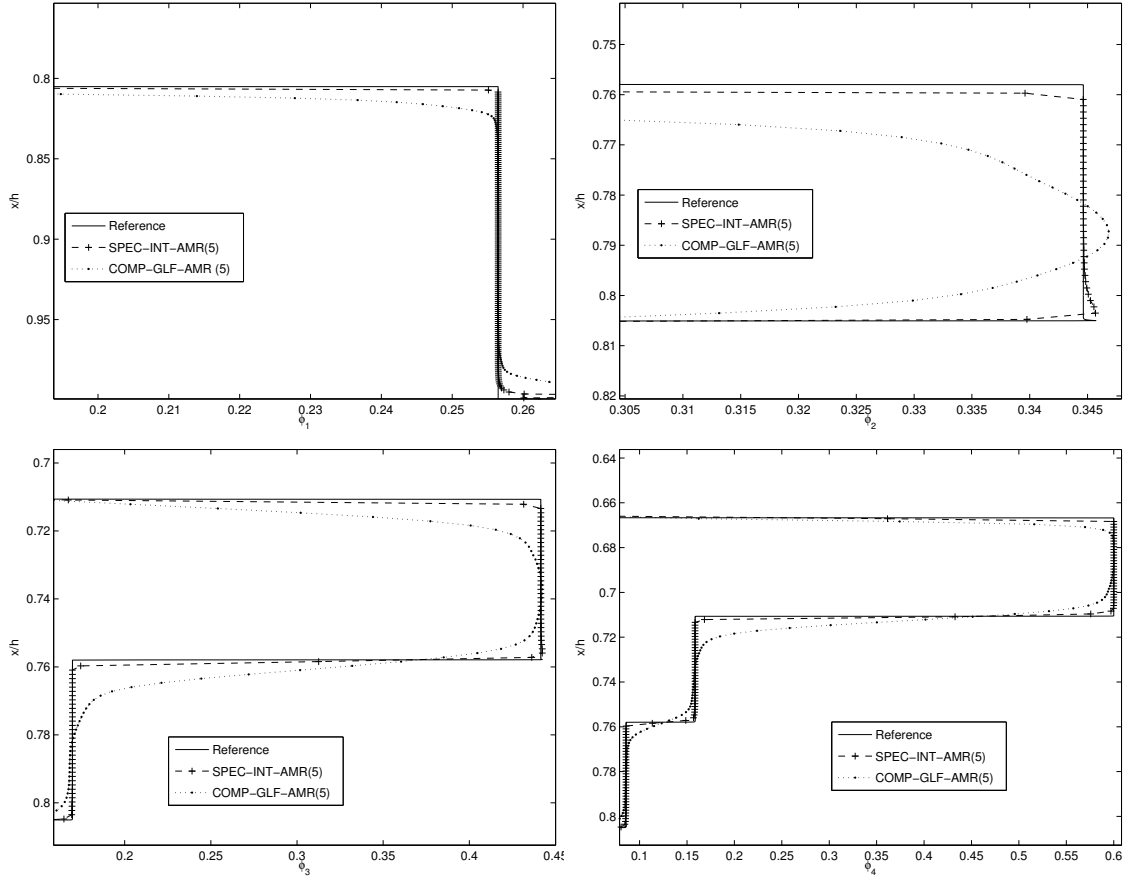


**Fig. 3** Example 1 ( $N = 4$ ): details of numerical solution at time  $t = 300$  s obtained by SPEC-INT-AMR and COMP-GLF-AMR methods with a grid hierarchy of  $L + 1 = 5$  levels on a coarsest grid with  $N_0 = 50$  subintervals.

**Table 1** Example 1 ( $N = 4$ ): Percentage of storage space (memory) and number of integrations of the adaptive algorithm with respect to the fixed grid algorithm with  $\tau_p = 10^{-2}$  at simulated time  $t = 50$  s, for a hierarchy of  $L + 1 = 5$  levels and four different values of  $N_0$ .

Fixed grid size ( $= N_0 \cdot 2^4$ )	SPEC-INT-AMR(5)		COMP-GLF-AMR(5)	
	% Integrations	% Memory	% Integrations	% Memory
800	25.20	21.92	29.70	24.75
1600	13.61	12.39	15.05	13.91
3200	6.88	6.66	7.84	7.61
6400	3.68	3.66	21.50	12.37

from coarse to fine elsewhere. A few enlarged views of relevant parts of the numerical solutions shown in Figures 2 and 3 illustrate that the algorithm correctly identifies the regions corresponding to the shocks. The percentage of the number of integrations of the AMR algorithm with respect to a solution on the uniform finest grid with  $N_4$  subintervals is 25.20% and 29.70% for the SPEC-INT-AMR and COMP-GLF-AMR methods, respectively, for this experiment.

In Table 1, we present the percentages of the number of integrations and storage space required by AMR with respect to schemes on the uniform finest mesh for constant tolerance  $\tau_p = 10^{-2}$ . The indicated percentage represents the average memory load over all iterations. The values of the table correspond to coarsest grids of  $N_0 = 50, 100, 200$  and  $400$  subintervals and  $L + 1 = 5$  levels of refinement. We observe that the percentage of memory allocated by the SPEC-INT-AMR and COMP-GLF-AMR codes decreases as  $N_0$  increases, as expected. However, we observe that for COMP-GLF-AMR code with  $N_0 = 400$ , which corresponds to a uniform grid of 6400 subintervals, both percentages increase. This phenomenon is probably due to spurious oscillations in the piecewise constant part of the solution produced by COMP-GLF. These oscillations do not disappear upon mesh refinement, as was observed in [7].

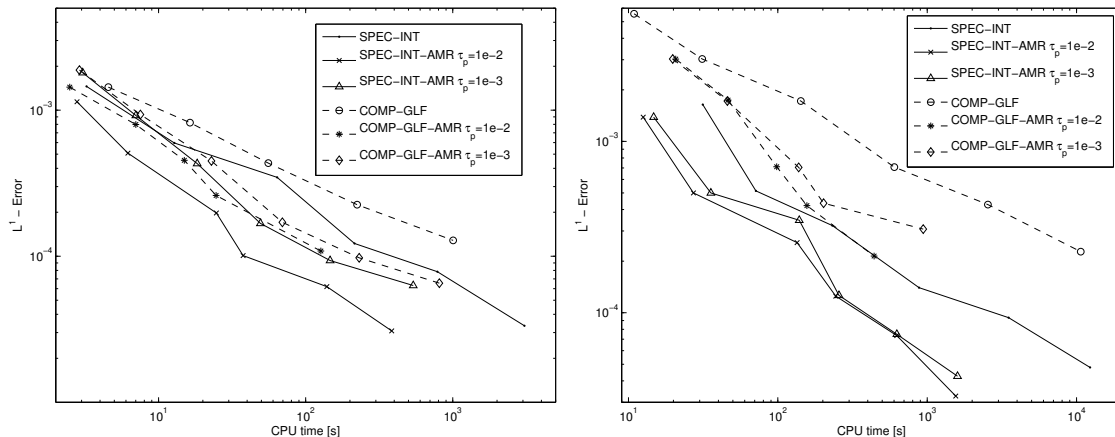


**Fig. 4** Example 1 ( $N = 4$ ): approximate  $L^1$  errors versus CPU time for SPEC-INT-AMR and COMP-GLF-AMR for different values of  $\tau_p$  at simulated times  $t = 50$  s (left) and  $t = 300$  s (right). Here and in Figure 6, for each scheme the interpolated symbols correspond to different values of  $N_0$ , and the AMR versions have been implemented with  $L + 1 = 4$  levels of refinement.

**Table 2** Example 2: Initial conditions  $\phi_i^0$ , real particle sizes  $d_i$  and normalized squared particle sizes  $\delta_i$ .

$i$	1	2	3	4	5	6	7
$\phi_i^0 [10^{-2}]$	0.2365	1.1039	3.5668	3.8776	6.0436	10.8998	4.2718
$d_i [10^{-5} \text{ m}]$	290	250	210	170	130	90	50
$\delta_i$	1.000000	0.743163	0.524376	0.343639	0.200951	0.0963	0.029727

In Figure 4, we show approximate  $L^1$  errors and CPU times at two different times for the SPEC-INT-AMR and COMP-GLF-AMR methods using a grid hierarchy for different levels and for the SPEC-INT and COMP-GLF methods using a fixed uniform grid. It turned out that the AMR technique is around ten times faster than the equivalent fixed-grid computation in many cases. This CPU time may be shorter if the depth  $L$  of the grid hierarchy is increased. For a given base resolution  $N_0$  and hierarchy depth  $L$ , we observe that COMP-GLF-AMR is faster than SPEC-INT-AMR (as should be expected, since the former scheme avoids the costly computation of the spectral decomposition of the flux Jacobian), but the latter gives results that are much closer to the reference solution. We plotted different choices for the threshold value  $\tau_p$  and observe that, for this case, the choice  $\tau_p = 10^{-2}$  gives the best efficiency.

#### 4.2 Example 2 ( $N = 7$ )

This example is based on experimental data from [14], where the settling of suspension in a column of height  $h = 0.227$  m was considered. The initial concentrations  $\phi_i^0$ , diameters  $d_i$  and normalized diameters  $\delta_i = d_i/d_1$  are given in Table 2. The maximum total concentration is  $\phi_{\max} = 0.6$  and the hindered settling factor is given by (2.2) with the exponent  $n_{\text{RZ}} = 5$ .

We simulate the process until the phenomenon enters in a steady state. Figs 5 shows the numerical solution obtained with SPEC-INT-AMR as concentration profiles at four different times together with the corresponding grid hierarchy. We have used a grid hierarchy of  $L + 1 = 6$  levels with a coarsest grid of  $N_0 = 50$  points so that results are comparable with those for a fixed grid of  $N_5 = 1600$  points. The tolerance for the interpolation error sensor has been set to  $\tau_p = 10^{-2}$ . The plotted positions indicate that the adaptive mesh refinement technique works correctly, in the sense that the scheme detects the shock formation and refines these areas.

In Figures 7 we show enlarged views of relevant parts of the numerical solutions for individual concentration and compare the results obtained at times  $t = 400$  s by SPEC-INT-AMR method with a grid hierarchy of  $L + 1 = 6$  levels on a coarsest grid with  $N_0 = 50$ , and SPEC-INT method on a fixed grid with  $N_0 = 1600$ , with a reference solution computed by SPEC-INT on a fixed grid with  $N_{\text{ref}} = 25600$  subintervals. The tolerance for the interpolation error sensor has been set to  $\tau_p = 10^{-2}$ . The percentage of integrations of the algorithm with respect to the solution on the finest grid is a 16.88% and the percentage of memory allocated by AMR technique is only 14.62% of the amount of memory allocated after each iteration of the coarse grid.

The error in the  $L^1$ -norm between the adaptive scheme for different  $L^1$  levels and the corresponding scheme on an equivalent uniform fine grid is depicted in Figure 6. From that figure we infer that the adaptive techniques SPEC-INT-AMR and COMP-GLF-AMR are always cheaper in CPU time than SPEC-INT and COMP-GLF methods on the finest grid. The

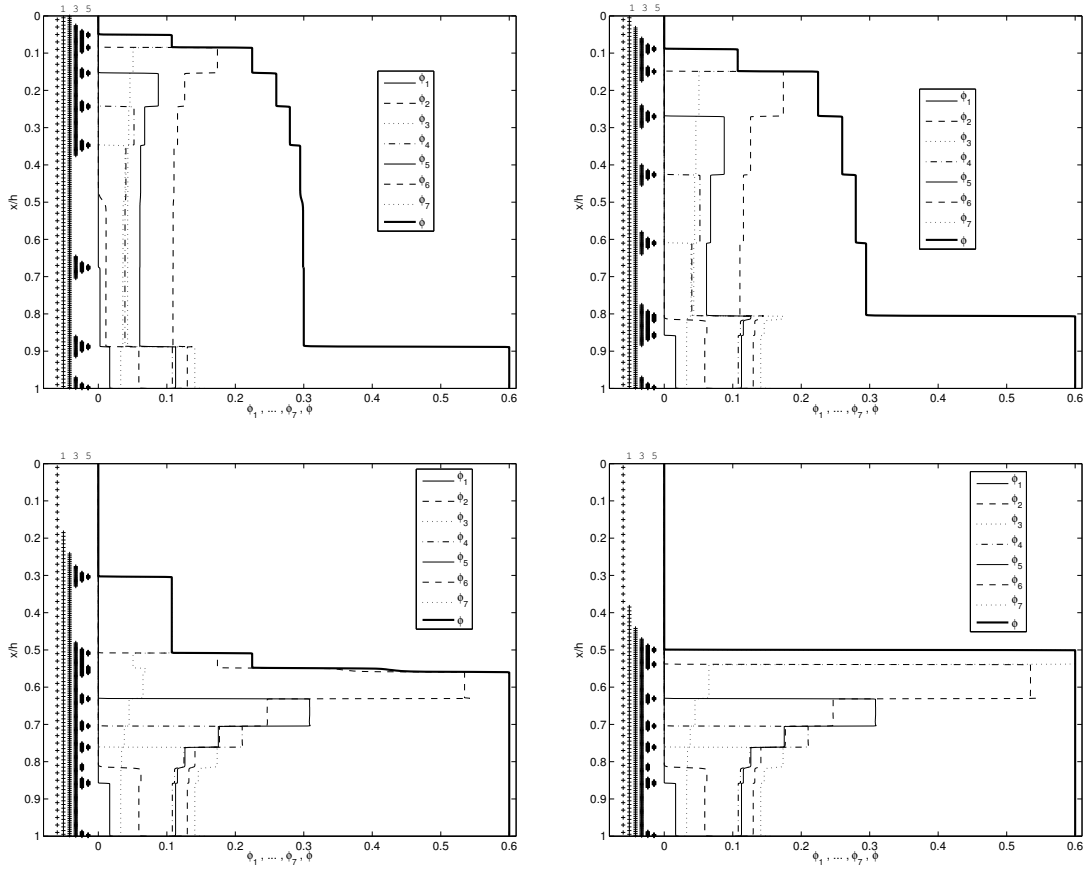


**Fig. 5** Example 2. ( $N = 7$ ): numerical solutions obtained with SPEC-INT-AMR with  $L + 1 = 6$  levels with coarsest grid of  $N_0 = 50$  subintervals at  $t = 228.05$  s (top left),  $t = 400$  s (top right),  $t = 1286.94$  s (bottom left) and  $t = 2500$  s (bottom right).

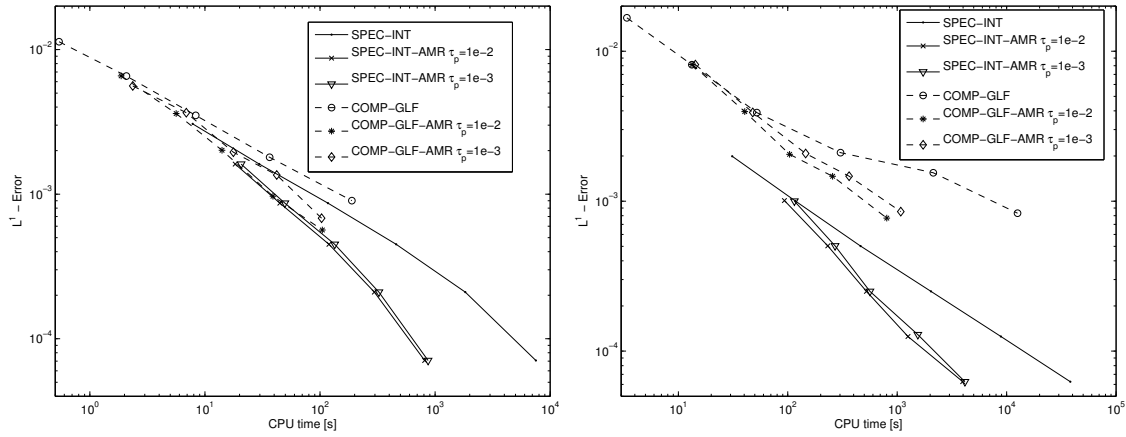


**Fig. 6** Example 2 ( $N = 7$ ): approximate  $L^1$  errors versus CPU time for SPEC-INT-AMR and COMP-GLF-AMR for different values of  $\tau_p$  at simulated times  $t = 400$  s (left) and  $t = 2500$  s (right).

reference solution was computed with SPEC-INT scheme on a fixed grid with 12800 subintervals at times  $t = 400$  s and  $t = 2500$  s. The CPU time used with adaptive technique is roughly a tenth of the CPU time required for the equivalent uniform grid. This CPU time can further be less when we use more levels. We plotted different choices for the threshold value  $\tau_p$  and observe that  $\tau_p = 10^{-2}$  is the most efficient choice.

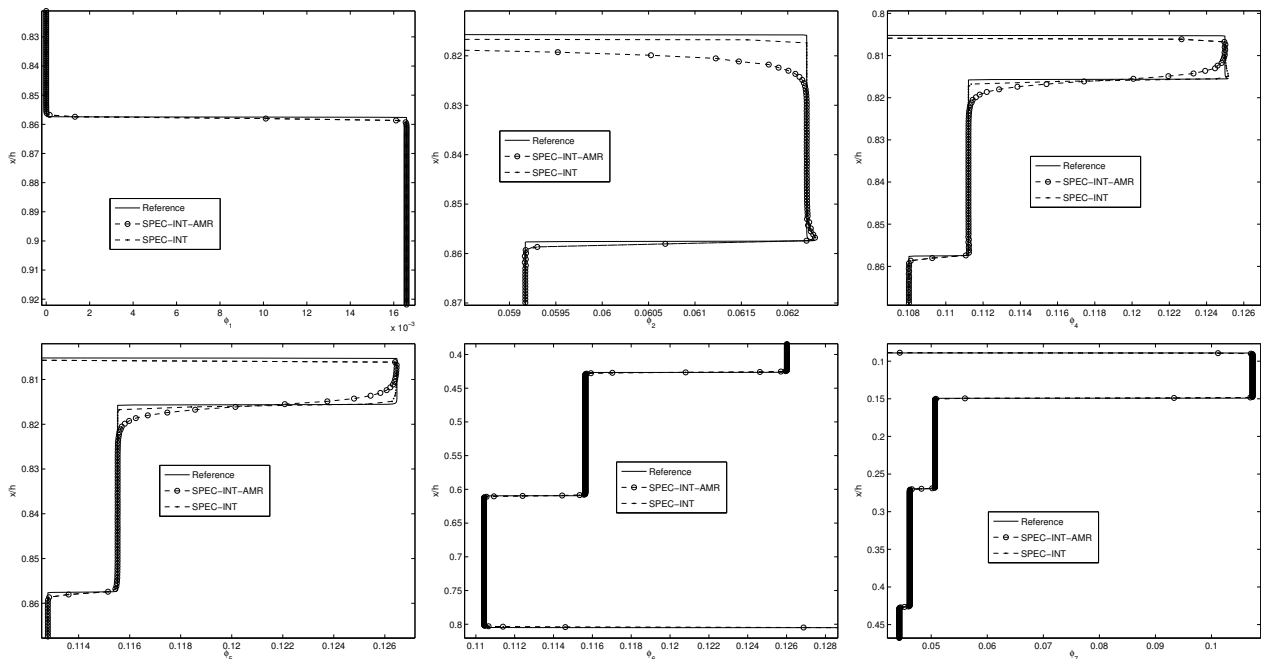


**Fig. 7** Example 2 ( $N = 7$ ): details of the numerical solution of the top right plot of Figure 5 for  $\phi_1$  (top left),  $\phi_2$  (top middle),  $\phi_4$  (top right),  $\phi_5$  (bottom left),  $\phi_6$  (bottom middle) and  $\phi_7$  (bottom right). In addition, the solution produced by SPEC-INT on a fixed grid with 1600 subintervals and the reference solution computed by SPEC-INT on a fixed grid with  $N_{\text{ref}} = 12800$  is shown.

### 4.3 Conclusions

We have applied an adaptive mesh refinement algorithm to save computational resources in simulations of polydisperse sedimentation by two state-of-the-art high resolution shock capturing techniques. In our experiments with 4 and 7 species and a given CPU time, the scheme that utilizes the characteristic information obtained through the use of the secular equation is more efficient than the scheme that makes no use of this information.

### Acknowledgments

R. Bürger acknowledges partial support by Fondecyt project 1090456, BASAL project CMM, Universidad de Chile and Centro de Investigación en Ingeniería Matemática (CI<sup>2</sup>MA), Universidad de Concepción. P. Mulet acknowledges support by Spanish MICINN projects MTM 2008-00974 and MTM 2011-22741. L.M. Villada acknowledges support by MECESUP project UCO0713.

### References

- [1] J. Anderson, A secular equation for the eigenvalues of a diagonal matrix perturbation, *Lin. Alg. Appl.* **246**, 49–70 (1996).
- [2] A. Baeza, A. Martínez-Gavara, and P. Mulet, Adaptation based on interpolation errors for high order mesh refinement methods applied to conservation laws, *Appl. Numer. Math.*, in press.
- [3] M.J. Berger and P. Colella, Local adaptive mesh refinement for shock hydrodynamics, *J. Comput. Phys.* **82**, 64–84 (1989).
- [4] M.J. Berger and J. Olinger, Adaptive mesh refinement for hyperbolic partial differential equations, *J. Comput. Phys.* **53**, 484–512 (1984).
- [5] S. Berres, R. Bürger, K.H. Karlsen, and E.M. Tory, Strongly degenerate parabolic-hyperbolic systems modeling polydisperse sedimentation with compression, *SIAM J. Appl. Math.* **64**, 41–80 (2003).
- [6] R. Bürger, R. Donat, P. Mulet, and C.A. Vega, Hyperbolicity analysis of polydisperse sedimentation models via a secular equation for the flux Jacobian, *SIAM J. Appl. Math.* **70**, 2186–2213 (2010).
- [7] R. Bürger, R. Donat, P. Mulet, and C.A. Vega, On the implementation of WENO schemes for a class of polydisperse sedimentation models, *J. Comput. Phys.* **230**, 2322–2344 (2011).
- [8] R. Bürger, R. Donat, P. Mulet, and C.A. Vega, On the hyperbolicity of certain models of polydisperse sedimentation, *Math. Meth. Appl. Sci.*, to appear.
- [9] R. Bürger, K.H. Karlsen, E.M. Tory, and W.L. Wendland, Model equations and instability regions for the sedimentation of polydisperse suspensions of spheres, *ZAMM Z. Angew. Math. Mech.* **82**, 699–722 (2002).

- [10] R. Bürger and A. Kozakevicius, Adaptive multiresolution WENO schemes for multi-species kinematic flow models, *J. Comput. Phys.* **224**, 1190–1222 (2007).
- [11] G. Chiavassa and R. Donat, Point-value multiscale algorithms for 2D compressible flows, *SIAM J. Sci. Comput.* **20**, 805–823 (2001).
- [12] A. Cohen, S. Kaber, S. Müller, and M. Postel, Fully adaptive finite volume schemes for conservation laws, *Math. Comp.* **72**, 183–225 (2003).
- [13] R. Donat and P. Mulet, A secular equation for the Jacobian matrix of certain multi-species kinematic flow models, *Numer. Methods Partial Differential Equations* **26**, 159–175 (2010).
- [14] R.M. Dorrell, A.J. Hogg, E.J. Sumner, and P.J. Talling, The structure of the deposit produced by sedimentation of polydisperse suspensions, *J. Geophys. Res.* **116**, paper F01024 (2011).
- [15] A. Harten, Multiresolution algorithms for the numerical solution of hyperbolic conservation laws, *Comm. Pure Appl. Math.* **48**, 1305–1342 (1995).
- [16] K. Höfler and S. Schwarzer, The structure of bidisperse suspensions at low Reynolds numbers. In: A.M. Sändig, W. Schiehlen and W.L. Wendland (eds.), *Multifield Problems: State of the Art*, Springer Verlag, Berlin, 42–49 (2000).
- [17] C. Hu, *Numerical Methods for Hyperbolic Equations on Unstructured Meshes*. PhD Thesis, Brown University, 1999.
- [18] A. Kurganov and E. Tadmor, New high-resolution central schemes for nonlinear conservation laws and convection-diffusion equations, *J. Comput. Phys.* **160**, 241–282 (2000).
- [19] P.D. Lax and B. Wendroff, Systems of conservation laws, *Comm. Pure Appl. Math.* **13**, 217–237 (1960).
- [20] J. Liandrat, The wavelet transform; some applications to fluid dynamics and turbulence, *Eur. J. Mech. B/Fluids* **9**, 1–19 (1990).
- [21] M.J. Lockett and K.S. Bassoon, Sedimentation of binary particle mixtures, *Powder Technol.* **24**, 1–7 (1979).
- [22] J.H. Masliyah, Hindered settling in a multiple-species particle system, *Chem. Eng. Sci.* **34**, 1166–1168 (1979).
- [23] J.J. Quirk, *An Adaptive Grid Algorithm for Computational Shock Hydrodynamics*. PhD Thesis, Cranfield Institute of Technology, 1991.
- [24] J.F. Richardson, W.N. Zaki, Sedimentation and fluidization: Part I, *Trans. Instn. Chem. Engrs. (London)* **32**, 35–53 (1954).
- [25] F. Rosso and G. Sona, Gravity-driven separation of oil-water dispersions, *Adv. Math. Sci. Appl.* **11**, 127–151 (2001).
- [26] C.-W. Shu and S. Osher, Efficient implementation of essentially non-oscillatory shock-capturing schemes, *J. Comput. Phys.* **77**, 439–471 (1988).
- [27] H. Tang and T. Tang, Adaptive mesh methods for one- and two-dimensional hyperbolic conservation laws, *SIAM J. Numer. Anal.* **41**, 487–515 (2004).

# Centro de Investigación en Ingeniería Matemática (CI<sup>2</sup>MA)

## PRE-PUBLICACIONES 2011

- 2011-19 ANA ALONSO-RODRIGUEZ, JESSIKA CAMAÑO, ALBERTO VALLI: *Inverse source problems for eddy current equations*
- 2011-20 RODOLFO RODRÍGUEZ, PABLO VENEGAS: *Numerical approximation of the spectrum of the curl operator*
- 2011-21 JULIO ARACENA, JACQUES DEMONGEOT, ERIC FANCHON, MARCO MONTALVA: *On the number of update digraphs and its relation with the feedback arc sets and tournaments*
- 2011-22 RAIMUND BÜRGER, ROSA DONAT, PEP MULET, CARLOS A. VEGA: *On the hyperbolicity of certain models of polydisperse sedimentation*
- 2011-23 GABRIEL N. GATICA, ANTONIO MARQUEZ, SALIM MEDDAHI: *Analysis of an augmented fully-mixed finite element method for a three-dimensional fluid-solid interaction problem*
- 2011-24 GABRIEL N. GATICA, NORBERT HEUER, SALIM MEDDAHI: *Coupling of mixed finite element and stabilized boundary element methods for a fluid-solid interaction problem in 3D*
- 2011-25 CAROLINA DOMINGUEZ, GABRIEL N. GATICA, SALIM MEDDAHI, RICARDO OYARZÚA: *A priori error analysis of a fully-mixed finite element method for a two-dimensional fluid-solid interaction problem*
- 2011-26 FABIÁN FLORES-BAZÁN, SIGIFREDO LAENGLE, GINO LOYOLA: *Characterizing the efficient points without closedness or free-disposability*
- 2011-27 JORGE CLARKE, CIPRIAN A. TUDOR: *Least squares estimator for the parameter of the fractional Ornstein-Uhlenbeck sheet*
- 2011-28 ANAHI GAJARDO, JARKKO KARI, ANDRES MOREIRA: *On time-symmetry in cellular automata*
- 2011-29 TOMÁS BARRIOS, ROMMEL BUSTINZA, GALINA C. GARCÍA, ERWIN HERNÁNDEZ: *A stabilized mixed method for generalized Stokes problem based on the velocity-pseudo-stress formulation: A priori error estimates and an optimal control problem*
- 2011-30 RAIMUND BÜRGER, PEP MULET, LUIS M. VILLADA: *Spectral WENO schemes with adaptive mesh refinement for models of polydisperse sedimentation*

Para obtener copias de las Pre-Publicaciones, escribir o llamar a: DIRECTOR, CENTRO DE INVESTIGACIÓN EN INGENIERÍA MATEMÁTICA, UNIVERSIDAD DE CONCEPCIÓN, CASILLA 160-C, CONCEPCIÓN, CHILE, TEL.: 41-2661324, o bien, visitar la página web del centro: <http://www.ci2ma.udec.cl>



**CENTRO DE INVESTIGACIÓN EN  
INGENIERÍA MATEMÁTICA (CI<sup>2</sup>MA)  
Universidad de Concepción**



Casilla 160-C, Concepción, Chile  
Tel.: 56-41-2661324/2661554/2661316  
<http://www.ci2ma.udec.cl>



---